



Water soluble graphitic carbon nitride with tunable fluorescence for boosting broad-response photocatalysis



Yongli Li^{a,b}, Peipei Li^a, Jinshu Wang^{a,*}, Yilong Yang^a, Wenqing Yao^b, Zhen Wei^b, Junshu Wu^b, Xiaoxiao Yan^a, Xiangfeng Xu^a, Yuhan Liu^a, Yongfa Zhu^{b,*}

^a College of Materials Science & Engineering, Beijing University of Technology, Beijing 100124, China

^b Department of Chemistry, Beijing Key Laboratory for Analytical Methods and Instrumentation, Tsinghua University, Beijing 100084, China

ARTICLE INFO

Keywords:

Carbon nitride
Water-solubility
Fluorescence
Photocatalysts
Band engineering

ABSTRACT

A one-step salt melt assisted thermal polymerization for the synthesis of nitrogen-rich water soluble graphitic carbon nitride (WS-GCN) is presented. The as-prepared WS-GCN shows strong tunable excitation-emission pathways that have multi-colored photoluminescence from blue to green with extremely high absolute quantum yields (AQY) of 22%, which is almost 6 fold of pristine graphitic carbon nitride (GCN) nanosheets. It also shows significant red-shift of response edge benefiting from the narrowed band energy, due to the feature of N-defected surface and N-rich inner of WS-GCN. After being decorated onto TiO₂, the WS-GCN endows a great enhancement of NO-photodegradation under visible light irradiation, 5.5-fold increase to comparison with what the pristine GCN does. Further, the starting edge of photocatalysis is enlarged to about 650 nm for TiO₂/WS-GCN from about 450 nm for TiO₂/GCN. This is ascribed to both enhanced light-response range and efficiently restraining the radiative transition probability of WS-GCN owing to the migration of photoinduced electrons from the CB of WS-GCN to TiO₂. This multi-functional material may provide a way for the development of bio-imaging, file secrecy and broad absorption photocatalysts.

1. Introduction

Graphitic carbon nitride (g-C₃N₄) has caught many eyes as a non-metallic semiconductor polymer, owing to its intriguing 2D layered molecular structure, high thermal/chemical stability, favorable biocompatibility, manageable band gap as well as the earth-abundant compositions [1–4]. These distinct characteristics endow it novel and unique properties in photocatalysis [5–9], fluorescence sensing [10–14], biomedical imaging [15–18] and phototherapy [19,20]. In particular, the manipulability of g-C₃N₄ in elementary compositions and electronic structures is extremely important both fundamentally and technologically. Benefiting from the adaptive VB (~1.1 eV at the top) and CB (~−1.6 eV at the bottom) level for redox of water, g-C₃N₄ stands out from photocatalysts in water splitting, organic pollutant degradation and artificial photosynthesis. Generally, g-C₃N₄ can be synthesized facilely by thermal polymerization of nitrogen-rich molecular precursors, typically including melamine [21], dicyanamide [22], cyanamide [23] and urea [24]. However, the photocatalytic activity of pristine g-C₃N₄ suffers from a fast recombination rate of photo-generated carriers and a limited visible-light absorption range, which shows bright blue fluorescence (ca. centered at ~460 nm) arising from

delocalized π^{*}-n radiative transition, corresponding to around 2.7 eV [10,25,26]. In this context, various strategies have been explored to surmount these problems [27–30]. Recently, developments have been reached by intercalating or exfoliating the bulk g-C₃N₄ into the atomic thickness or quantum dot scale, which is conducive to shuttle the photoexcited electrons and shorten the migration distance to the surface of g-C₃N₄ [31]. Xu et al. [32] developed a H₂SO₄-intercalation approach to single-layered g-C₃N₄ sheets, and 3-fold enhancement in photocatalytic H₂ evolution was obtained. Niu et al. [33] provided a controllable thermal oxidation process to etch bulk g-C₃N₄ into a few atomic layers that exhibits illustrating superior photocatalytic activity owing to the improved electron transport ability and prolonged electron life-time. Simply by ultrasonic treatment, bulk g-C₃N₄ can also be exfoliated into atomic-thick nanosheets, at the cost of broadening band gap due to the quantum confinement effect by shifting the conduction and valence band edges in opposite directions. To extend the light absorption range of g-C₃N₄, the graft copolymerization [34–37], amorphization (R-melon) [38], heteroatoms doping, such typical foreign atoms as B [39,40], S [40–43], P [44,45], K [46–48], halogens [49,50], and N-rich [51,52] or N-defect [10,47,53–57], were recently developed to narrow its band gap. However, preparation of soluble g-

* Corresponding authors.

E-mail addresses: lyl@bjut.edu.cn (Y. Li), wangjs@bjut.edu.cn (J. Wang), zhuyf@mail.tsinghua.edu.cn (Y. Zhu).

C_3N_4 and solvation of $\text{g-C}_3\text{N}_4$ is still a challenge. Although small $\text{g-C}_3\text{N}_4$ nanoparticles (Quantum Dots) show strong blue photoluminescence (PL), definitive experimental evidence for optical property manipulation of $\text{g-C}_3\text{N}_4$ building blocks arising from quantum-confinement effects and defect-dependence of $\text{g-C}_3\text{N}_4$ remains scarce [17].

Herein, we develop a one-step binary melt salts-assisted (KCl-NaCl) method toward tailoring the morphology, size and defects of $\text{g-C}_3\text{N}_4$ (WS-GCN) that possess excellent dependent photoluminescence (PL) properties, band engineering and water-solubility. Significantly, we demonstrate the design of photocatalysts ($\text{TiO}_2/\text{WS-GCN}$ composite system) to harness the use of near the full spectrum of sunlight, based on significantly narrowing band gap of carbon nitride.

2. Experimental

2.1. Synthetic procedures

2.1.1. Synthesis of the water soluble $\text{g-C}_3\text{N}_4$

6 g of dicyandiamide and a given amount of alkali halides containing NaCl and KCl with molar ratio of 1:1 were dissolved in 200 mL of deionized water. dehydration was then performed applying vacuum-rotary evaporation procedure, followed by drying at 60 °C for overnight. The dried precursor was put into a corundum crucible with cover and wrapped up with aluminum foil, which were then heated at 670 °C for 45 min in static air with a rump-up rate of 2 °C/min. After cooling to room temperature, the product was dissolved in water, filtrated to remove the insoluble impurities and purified for several times using ethanol-water (1:2) mixed solvent. Finally, the purified product was re-dissolved into deionized water, denoted as WS-GCN. Pristine GCN was prepared by directly heating dicyandiamide at 670 °C for 45 min.

2.1.2. Synthesis of TiO_2 nanoparticles (NPs)

The anatase and brookite TiO_2 NPs were prepared by hydrothermal process according to the literature methods [58,59], respectively. for preparation of anatase TiO_2 NPs, 1 mL TiCl_4 was slowly dropped in 20 mL ethanol with constant stir to form a transparent colloidal solution, which was then sealed in a Teflon-lined stainless steel autoclave and kept at 200 °C for 24 h. for preparation of brookite TiO_2 NPs, 30 mL deionized water were poured in a Teflon autoclave, and 1 mL of TiCl_4 was cautiously added. After stirring for 10 min, 3.5 g of urea were dissolved in this solution. Finally, 3.3 mL of sodium lactate liquor were poured in the mixed solution. After another 30 min of stirring, the autoclave was sealed and put into an oven at 200 °C, holding for 12 h.

the above TiO_2 products were collected and washed with deionized water and ethanol for three times. After thoroughly dried, the products were burned at 350 °C for 2 h in static air to eliminate the residual organic species.

2.1.3. Synthesis of $\text{TiO}_2/\text{WS-GCN}$ photocatalyst

0.2 g of TiO_2 NPs were dispersed in 50 mL of deionized water and sonicated until a uniform suspension was obtained. a certain amount of WS-GCN were dissolved in 10 mL of water and dropped into the WS-GCN solution with vigorously stirring. Afterwards, the mixture was refluxed for 2 h at 60 °C, followed by adjusting to pH 1 using 1 M of HCl and centrifuging at a 5000 rpm and drying. The counterpart material, TiO_2/GCN , was also prepared according to the same procedure.

2.2. Characterizations

The crystal phase composition of products were performed by X-ray diffraction (XRD) with Cu K α radiation at a scan rate of 0.01° 2θ/s. Scanning electron microscopy (SEM) and Transmission electron microscopy (TEM) were used to observe the morphology and microstructure of the products in Hitachi S-8020U and JEM-2010 separately. The functional groups were analyzed through a PerkinElmer FT-IR spectrometer by the embed-in KBr pellets. Raman spectra were carried

in a DXR™2 Raman spectrometer. UV-vis absorption spectra was recorded by a Shimadzu UV-3600 plus. X-ray photoelectron spectra (XPS) was surveyed by the use of a PHI Quantera II system with an Al K_X-ray photoelectron spectrometer at 150 W. The C, N and H contents were analyzed with a Flash EA elemental analyzer. Edinburgh FLS980 Fluorescence spectrometer was employed to investigate the Photoluminescence (PL) properties of the products.

2.3. Electrochemical/Photoelectrochemical measurements

The photocurrent measurements were measured on a CHI 660 B electrochemical system, which use a standard three-electrode configuration. The working electrode was prepared using doctor blading method on an indium-tin oxide (ITO) glass electrode. The counter electrode and the reference electrode were a platinum wire and a saturated calomel electrode (SCE), respectively. 0.1 M of Na_2SO_4 (pH = 7) aqueous solution were used as the electrolyte. The visible light irradiation was obtained from a 300 W xenon lamp equipped with an AM1.5 filter and a 420 nm-cut off filter. For the preparation of working electrode, 50 mg of powder sample was mixed with 455 μL of ethanol and 5 μL of Nafion followed by sonication for 20 min to obtain a slurry. Then the slurry was dip-coated onto an 2 cm × 4 cm ITO glass on which an area of 1 cm^2 was exposed using Scotch tape protection. After removing the redundant slurry using doctor blade, the working electrode was dried in air at 80 °C for 12 h to form a well-adhered coating. The transient photocurrent curves were measured for 5 cycles of light on/off at 0 V vs SCE. The Mott-Schottky analysis was performed at a frequency of 1000 Hz by superimposing a 5 mV of AC amplitude on the DC applied potential, which varied from 0.5 to –0.5 V in steps of 50 mV with a time interval of 2 s.

2.4. Photocatalytic measurements

The photocatalytic activity was evaluated by degradation of gaseous NO under a given irradiation light in a continuous flow system with gas flow rate of 1 L/min. The input NO stream was obtained by diluting concentrate cylinder gas into 1 ppm using compressed air with 50% humidity. The detailed measurements were provided in our previous work [60]. The continuous detection of NO/NO_2 concentration was performed with a $\text{NO}-\text{NO}_2-\text{NO}_x$ gas analyzer (Thermo Scientific 42i-HL). The removal ratio (η , %) of NO was calculated using relationship $\eta = (1 - C_t/C_0) \times 100\%$, where C_0 and C_t are the outlet concentrations of NO before and after a certain time of photocatalytic reaction, which represent the feeding and residual NO, respectively.

3. Results and discussion

3.1. Diverse structures and optical properties of WS-GCN products

Fig. 1a–c and Fig. S1 display the TEM images of the WS-GCN products processed in different ratio of precursor to salts. The product obtained by 3:1 of precursor to salts dominantly exhibits a unique silk-like morphology with clear (002) spacing of $\text{g-C}_3\text{N}_4$ (0.34 nm) (Fig. 1a). Nevertheless, increasing the fractions of salts in precursor mixture produced significant change in morphologies, in which the crystal fringes are undistinguished, suggesting disordering of inter-layer π -stacking. Prepared in the ratio of 2:1, the product shows large-sized porous nanosheets with a few nanometers in thickness, and quantum dots became the main character by the ratio of 1:1 (Fig. 1b and c). These WS-GCN products were investigated by photoluminescence (PL) spectroscopy. All of the obtained WS-GCN show strong fluorescence under ultraviolet light (Fig. 1a–c, inset digital pictures). When increasing the ratio of melt salts to precursor, a distinct change of fluorescent color from bright blue to green can be observed at the fixed excitation wavelength of 365 nm, which were well depicted by PL spectra (Fig. 1d). The PL of WS-GCN at the same concentration (ca.

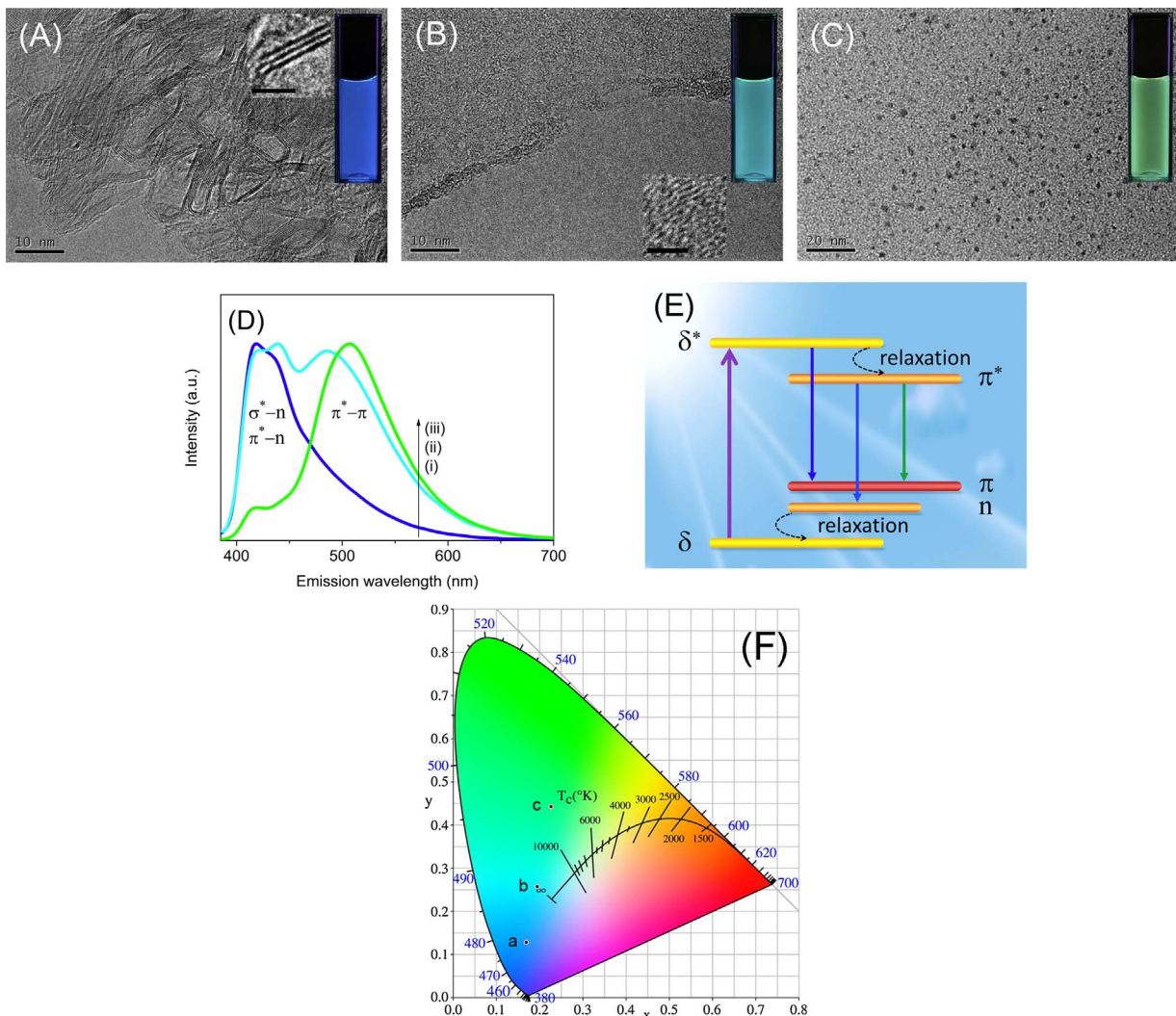


Fig. 1. TEM images of WS-GCN with different ratio of precursor to salts: (a) 3:1, (b) 2:1 and (c) 1:1, separately. Insets are the photographs showing lattice fringes (bar is 2 nm), and the digital pictures of fluorescence under excitation of 365 nm in fixed concentration of 0.5 mg/mL. (d) Normalized PL spectra of WS-GCN, in which the (i) blue, (ii) cyan and (iii) green lines correspond to (a)–(c). (e) Schematic diagram of the excitation-emission pathways of WS-GCN. (f) The Commission Internationale de l'Eclairage (CIE) chromaticity diagram of the WS-GCN products, where the point a, b and c represent the line (i)–(iii) of plot (d), respectively. (For interpretation of the references to colour in this figure legend, the reader is referred to the web version of this article.)

0.5 mg/mL) cover a wide range and show clear dual-color emission region, one of which is located between 420 and 440 nm (including the transition pathways of δ^* -n and π^* -n) and the other is centered in a range of 490–520 nm (referring to the π^* - π transition) (Fig. 1e) [10,26]. Although being intrinsically provided with same ternary excitation-emission pathways, the overwhelming transition pathway is assigned to δ^* -n and π^* -n for pristine GCN, resulting in blue-emission PL [24]. With respect to as-prepared WS-GCN, π^* - π transition was enhanced and red-shifted with increasing the proportion of melt salts, thereby altering the relative strength of emission models, which enable the materials to show color gradient, ca. blue, cyan, and green, as defined in the Commission Internationale de l'Eclairage (CIE) chromaticity diagram (Fig. 1f). Notably, the AQY reached up to 22% (measured with fluorescence spectrometer equipped integrating sphere) that is much higher than the value of pristine GCN nanosheets (3.7%) and most of reported results [2]. With illuminated under visible light (blue), even under sunlight excitation, well-marked green-colored PL of WS-GCN can also be observed (Fig. S2).

The unique PL features suggest a remarkable optical absorption properties of the as-obtained WS-GCN. As shown in Fig. 2a, UV-vis spectra exhibit a progressively extended absorption edge for the WS-GCN and an intensified absorbance under both UV and visible range

according to the ratio of precursor to salts. Correspondingly, the products display a change from brown to dark red (inset digital pictures in Fig. 2a). With compared to GCN, the absorption threshold of WS-GCN is significantly shifted by 176–341 nm towards the lower energy region to the maximum at 791 nm, which nearly cover across full visible spectrum. The holistic red-shift not only absorption-tailing indicates that photon excitation-recombination arises from band-to-band transition of electrons and reduced intrinsic bandgap. The depictions (Fig. 2b) with gradient edge of the transformed Kubelka-Munk function versus the photon energy exhibit a significant bandgap narrowing by 1.87 eV at the max., from 2.76 eV for GCN to 0.89 eV for WS-GCN (precursor: salts = 1:1). Similar products were synthesized by using melamine, cyanamide and urea as precursor, indicating the approach is robust for preparation of WS-GCN. Thus, we can conclude that the strong tunable emission of WS-GCN is close related to the narrowed band-gap radiative transition rather than the unsaturated surface bonding. These features endow the material with excellent optical applications such as bio-imaging, file secrecy field and broad-response photocatalysis.

As a promising metal-free photo/electro-catalyst and nontoxic biomarker, the insolubility of GCN remains one of the biggest impediments toward its potential applications. Previous research showed limited dispersible GCNs by long-time sonication [15], which were actually a

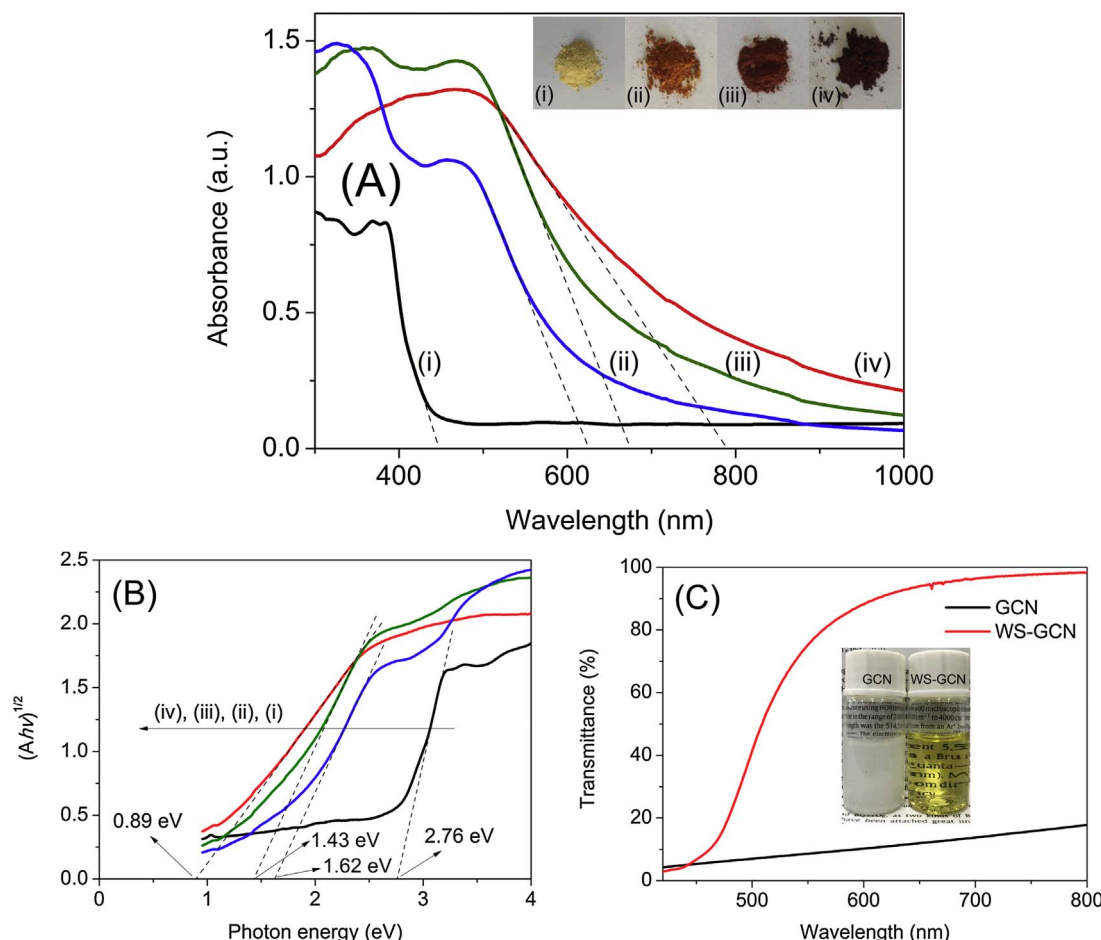


Fig. 2. (a) UV-vis diffuse reflection spectra and (b) $(Ahv)^{1/2}$ vs photon energy curve of bulk GCN and WS-GCN products, in which (i) is pristine GCN and (ii–iv) are the WS-GCN prepared at increasing ratio of precursor to salts, from 3:1 to 1:1, respectively. Insets in (a) are the corresponding digital pictures. (c) Transmittance spectra of pristine GCN nanosheets (supernatant liquid after 12 h-sonication of bulk GCN in water) and WS-GCN under visible light with same concentration (0.5 mg/mL), inset is the corresponding digital picture.

semi-translucent suspension and yielded low concentrations, usually lower than 0.2 mg/mL [11,15]. Other strategies that contained treating under harsh conditions such as high concentration of inorganic strong acid or alkali will be a challenge for operation and applications [3,4,61]. For all of our synthesized WS-GCN, the completely transparent solution were formed by pouring powder sample into water, without sono-treatment or addition of any dispersant (Fig. 2c). The average transmittance of WS-GCN reached to 72.12% in the range of 380–780 nm, while the pristine GCN was 8.82% under the same conditions, according to British Standard (EN 673). The color of solution progressively deepened from pale yellow to red with increasing concentration, showing well-defined Tyndall effect (Fig. S2 and S3, Supplementary Information). The concentration of WS-GCN solution can get up to 100 mg/mL, and there was no precipitation after a storage of six months in air at room temperature. In order to the formation of a stable colloidal solution without surfactant, it is well known that the Abs of Zeta potential must be over 30 mV. However, measurements illustrated that the WS-GCN are negatively charged with a surface potential between –8 and –11 mV. This surface potential is too small to provide sufficient electrostatic repulsion among particles for long-term stability. We suppose the strong hydrophilicity of WS-GCN enable them to dissolve into water, and may form hydrolysis layer on the surface, which might be ascribed to abundant dangling bonds and hydrophilic functional groups like C≡N on the edge of WS-GCN, confirmed by FT-IR and XPS analysis (refer to the details latter).

3.2. Compositions and chemical structures of WS-GCN

To explain the unique optical properties of WS-GCN products, we further conducted characterizations. Fig. 3a shows the X-ray diffraction (XRD) patterns of both GCN and the WS-GCN product. For pristine GCN, the strong peak at 27.82° represents the typical interplanar stacking aromatic systems of $\text{g-C}_3\text{N}_4$ layers in the (002) direction. The weaker XRD peak at 12.9° corresponds to the interplanar separation of tri-s-triazines, indexed as the (100) diffraction in the $\text{g-C}_3\text{N}_4$ crystal lattice. By contrast, the peak of (002) plane for WS-GCN becomes less pronounced and broader, revealing the decreased number of periodic stacking along (002) direction. Moreover, this peak slightly shifts by about 0.2° toward the smaller 2-theta degree (Fig. 3b), indicating the expansion of the periodic interlayer due to the amorphization and K-intercalation [47]. The (100) diffraction peak, which lies at 12.9° for GCN, is undetectable for WS-GCN, mainly caused by significantly reduced lateral size and absence of in-plane long-range order owing to the breaking of in-plane hydrogen bonds between strands of polymeric melon units [38,48]. This result is well coincident with TEM observations (Fig. 1).

The Fourier transform infrared spectroscopy (FT-IR), Raman spectra and X-ray photoelectron spectroscopy (XPS) analysis were performed to probe the chemical structures of WS-GCN. The characteristic FT-IR spectrum of WS-GCN is largely reminiscent of that of the bulk GCN (Fig. 4), both having peaks at 803 cm^{-1} (tri-s-triazine ring out of plane bending) and $1200\text{--}1800 \text{ cm}^{-1}$ ($\text{N}=\text{C}-\text{N}$ hetero-aromatic rings in the melon framework) [4,55,57]. However, changes are effortlessly found for the WS-GCN. The vibrations at 1639 ($\text{C}=\text{N}$), 1575 ($\text{C}=\text{N}$), 1450

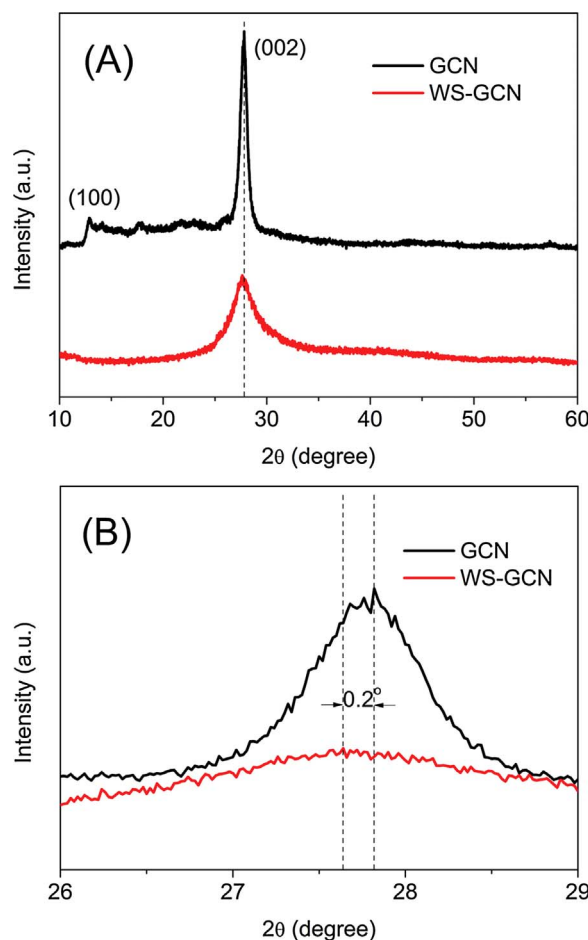


Fig. 3. (a) XRD patterns of bulk GCN and the WS-GCN, (b) enlarged XRD pattern of (a).

(C—N), 1406 (C—N) are retained for the WS-GCN, but the C—N peaks at 1461, 1318, 1238 and 1207 cm^{-1} show obvious shift or even disappearance with respect to those of bulk GCN. These differences became more pronounced with increasing salts fractions (Fig. S4, Supplementary Information), which reveals a vital information that the chemical bonding features about aromatic C—N network has changed. Those are in agreement with C 1s and N 1s XPS spectra (see Fig. 5). Moreover, a strong peak that appears at 2183 cm^{-1} corresponds to an asymmetric stretching vibration of cyano groups ($\text{C}\equiv\text{N}$) [13,47,55], together with the decreased intensity of tri-s-triazine characteristic peak, it suggests the ring-opening of triazine in heptazine framework. Additionally, an IR-absorption frequency (2145 cm^{-1}) close to the vibration of $\text{C}\equiv\text{N}$ might be caused by K-intercalation. In consideration of weak bonding between K^+ cation and N [46,48], K^+ could be easily substituted by H^+ through ion-exchange process, as shown in Fig. S5 (Supplementary Information), this peak disappeared after treatment using diluted acid. The results were confirmed by XPS analysis, as K (K2p) was detected to be 2.78% for raw WS-GCN and trace amount after treatment. Thus, we can infer this vibration peak is assigned to K—N bond. The Raman spectra of the GCN products have been recorded using the NIR 785 nm laser as excitation source (Fig. S6, Supplementary Information). The characterization peaks of GCN at 708 and 1232 cm^{-1} that are affiliated to heptazine ring breathing mode and stretching vibration modes of $\text{C}=\text{N}$ and C—N heterocycles, respectively, are undetectable with regard to WS-GCN, indicating low crystallinity and disturbance of strong fluorescence, which was confirmed by XRD and PL analysis. Moreover, Raman spectrum without the carbon related D and G bands suggest the absence of carbonized products in WS-GCN, even the employed temperature got up to 670 °C.

To reveal the exact position and elemental chemical state of WS-

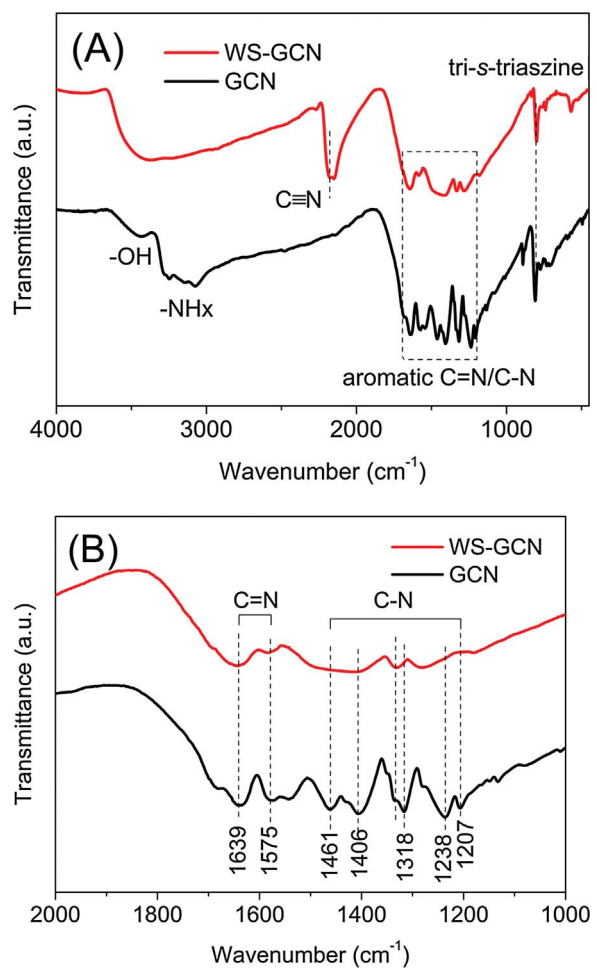


Fig. 4. (a) FT-IR spectrum of bulk GCN and the WS-GCN, (b) enlarged FT-IR pattern of (a).

GCN, we analyzed similarity and divergence of C 1s and N 1s XPS spectra for GCN and WS-GCN (Fig. 5). For both GCN and WS-GCN, the C 1s spectra can be deconvoluted into related Gaussian peaks, in which the three peaks from low to high binding energy (BE), 284.8, 286.6 and 288.1 eV (Fig. 5a), were ascribed to standard C—C bond related to aromatic carbon, amines on the edges of heptazine units and N=C—N coordination in the melon framework, respectively [3,47,55]. The BE at 289 eV for GCN may come from the surface carbon atoms bound to oxygen (C=O) in carboxylic [46], caused by slight oxidation of the g-C₃N₄ in air at high temperature. On the contrary, we could not make the C=O peak deconvoluted in the case of WS-GCN. The XPS survey detected about 9% of oxygen on the surface of GCN (Table S1, Supplementary Information), while trace amounts of oxygen were found on WS-GCN. It is reasonable to consider that the fresh condensed g-C₃N₄ was imbedded in the molten alkali halides at high temperature to be isolated from air, preventing from oxidation. According to the organic elemental analysis (OEA) (Table S1, Supplementary Information), C/N atomic ratio for pristine GCN is 0.683, close to the literature results for g-C₃N₄ [55], while the distinctively lower C/N (0.617) was found in WS-GCN, suggesting a N-rich structure for the bulk phase. Interestingly, XPS survey determined a C/N ratio of 1.022 for WS-GCN, which is in good agreement with the larger peak area centered at 284.8 eV to compare with the pristine GCN. It is more likely due to the surface N-defect of WS-GCN, rather than extrinsic carbon impurities. Additionally, since cyano groups (C≡N) share similar C1s BE with C bond to NH/NH₂ [55], it can be also taken as a reliable evidence for the formation of C≡N due to the substantial decline of N—H stretching according to FT-IR spectra. The N1s XPS spectrum for GCN contained

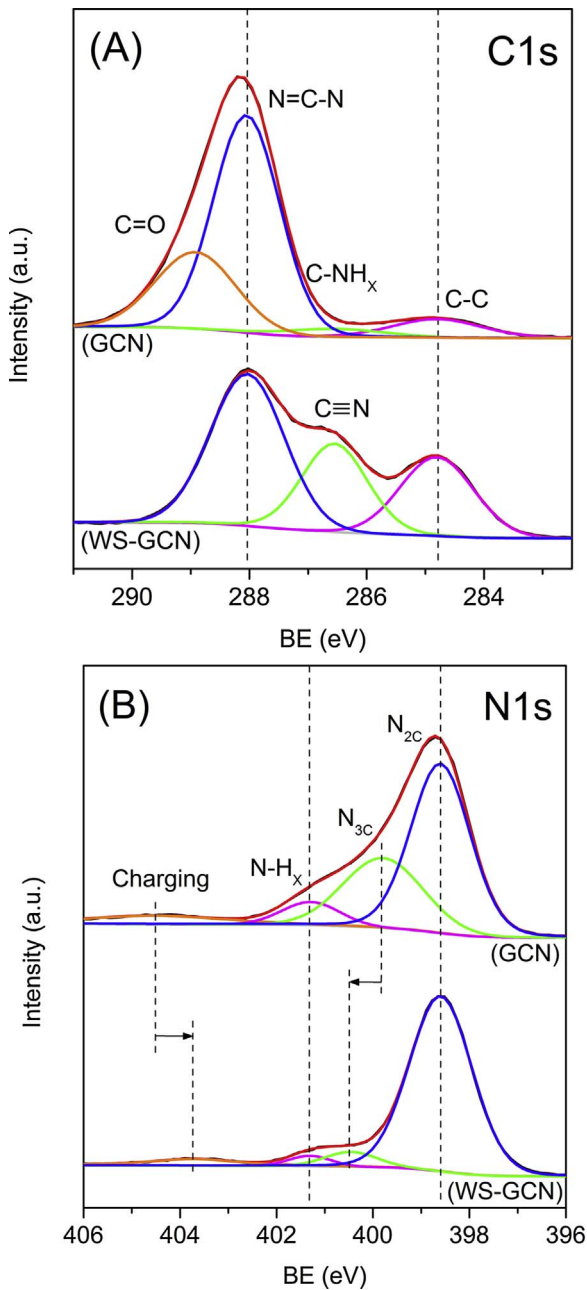


Fig. 5. (a) C1s and (b) N1s XPS spectra of GCN and WS-GCN.

three components at 398.6, 399.8, and 401.3 eV, assigned to the two-coordinated (N_{2C}) nitrogen atoms and the three-coordinated (N_{3C}) nitrogen atoms in the melon structure, as well as the NH_x (NH, NH_2) groups on the edge of the heptazine network (Fig. 5b) [55]. With de-polymerization of GCN and the surface N-defect by eutectic halide salts at high temperature, both N_{3C} and NH_x peaks remarkably weakened, and N_{3C} peak shifted to higher BE, probably because of presence of electron withdrawing groups such as $C\equiv N$. Further, the peak area of N_{3C} dramatically reduced, ca. N_{3C}/C_{total} atomic ratio drops from 0.58 to 0.093, strongly suggesting the formation of N_{3C} defects on the surface of WS-GCN. Furthermore, significantly increasing of N_{2C}/N_{3C} atomic ratios from 2.05 to 14.7 indicates that pyridinic-N is in dominance on the surface. Based on the above analysis, it is deduced that the as-prepared WS-GCN possesses a unique structure of N-rich inner and N-defect surface with abundant unsaturated dangling bonds, which is account for the attractive optical properties. The above results also suggest that the ionic liquid of KCl-NaCl at high temperature play a crucial role in

tailoring π -conjugated GCN molecules, not only for grain growth, but involves the dismembering of covalent *ab*-plane. We propose the possible formation process of WS-GCN as follows. At the earlier stage, pristine GCN forms by polycondensation of dicyandiamide precursor. When temperature increases to the melting point of the binary KCl-NaCl salts, ions in these molten salts are released from crystal lattice, which possess very highly chemical reactivity. K^+ and Cl^- can easily intercalate into the interplanar space of fresh condensed GCN and are adsorbed into the voids among bridged tris-*s*-triazines by the formation of K–N strong interaction [13], then cause the N-defects and rearrangement of tris-*s*-triazine units. Finally, bulk GCN is disintegrated and converted into diverse structures of WS-GCN that depends on the ratio of precursor to salts.

3.3. WS-GCN decorated TiO_2 ($TiO_2/WS\text{-}GCN$) with enhanced vis-driven photocatalytic activity

The above results suggest that as-prepared WS-GCN may be used as a powerful broad-responsed energy-transfer component in photocatalyst design for applications in environmental and energy issues. TiO_2 offers potentially a facile and inexpensive method for removing environmental pollutants, but suffers from the inefficient use of sunlight or visible light as irradiation source, because of large intrinsic band gap of undoped TiO_2 . In view of the well matched band alignment between GCN and TiO_2 [60], we expected that combining WS-GCN with catalytic TiO_2 in a composite system for photocatalysis would realize the efficient usage of the broad visible spectrum of sunlight. As shown in Fig. 6a-b and Fig. S7, it shows unchanged morphologically with low magnification before and after combining WS-GCN, and no diffraction peaks from WS-GCN were observed in the composite because of the small amount (3 wt.%) as well as the low diffraction intensity of WS-GCN (Fig. 6c). When observed under large magnification, the turbostratic layers wrapped on the surface of TiO_2 NPs are easily discernible (Fig. 6b). We changed optionally observation area, and found that the WS-GCN coating of a few atomic thickness is ubiquitous and well distributed (Fig. S8). Seen from FTIR spectra of TiO_2 , WS-GCN and $TiO_2/WS\text{-}GCN$ (Fig. 6d), the characteristic vibrations of WS-GCN, $N=C-N$ hetero-aromatic rings at $1200\text{--}1800\text{ cm}^{-1}$ and $C\equiv N$ groups at 2183 cm^{-1} , were also found in the $TiO_2/WS\text{-}GCN$ composite. Thus, it can be defined that the $TiO_2/WS\text{-}GCN$ is of a core-shell nanostructure, forming an intimate contact between WS-GCN shell and TiO_2 NPs. Considering the morphological change of raw WS-GCN used here (QDs) and the one in the composite (Fig. 1c), we inferred that self-assembly of WS-GCN molecules occurred during mixing of TiO_2 NPs and WS-GCN in aqueous, owing to spontaneously decreasing of surface free energy and soft 2D molecule of WS-GCN. Nitrogen adsorption-desorption isotherms show characteristic type-II curves accompanied by a H_3 -type hysteresis loop for TiO_2 NPs, $TiO_2/WS\text{-}GCN$ and WS-GCN, with BET surface area of 77.19, 56.83 and $3.97\text{ cm}^2/\text{g}$, respectively (Fig. 6e). It is worth noting that raw WS-GCN has a fairly small surface area, indicating strong driving force toward aggregations when precipitating from un-passivated WS-GCN QDs aqueous, which was demonstrated by SEM observations (Fig. S9). Fig. 6f shows the UV-vis diffuse reflection spectra of TiO_2 , WS-GCN and $TiO_2/WS\text{-}GCN$, which indicates the light response edge was expanded from 385 nm (TiO_2) to 600 nm with a long tail, owing to the incorporation of WS-GCN, while the GCN contributed much smaller to visible light harvest (460 nm). To further understanding the interaction between WS-GCN and TiO_2 NPs, we analyzed XPS of $TiO_2/WS\text{-}GCN$, as shown in Fig. 7. It can be seen in Fig. 7a-c, the BE of $N=C-N$ and N_{2C} exhibit a slight shift to the higher energy (by 0.1–0.3 eV) in comparison to raw WS-GCN, while those of Ti 2p shift to the lower energy by about 0.4 eV (vs TiO_2 NPs). Furthermore, surface $Ti-OH$ (530.8 eV) becomes unpronounced after WS-GCN decorating, probably attributed to the replacement of surface $-OH$ by WS-GCN (Fig. 7d). These results suggest a charge transfer from WS-GCN to TiO_2 owing to the strong $\pi\text{-}d$ interaction [62], which will favors to the fast

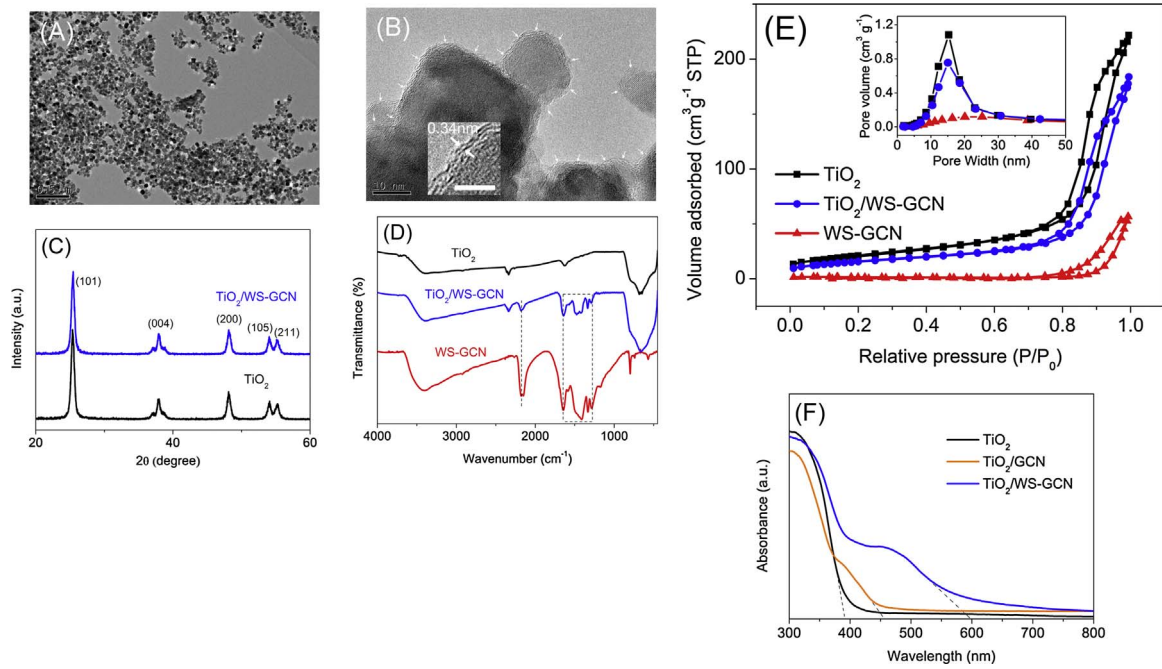


Fig. 6. (a) and (b) TEM images for $\text{TiO}_2/\text{WS-GCN}$ (bar is 2 nm), (c) XRD of TiO_2 and $\text{TiO}_2/\text{WS-GCN}$, (d) FTIR, (e) Nitrogen adsorption-desorption isotherms and (f) UV-vis diffuse reflection spectra of TiO_2 , WS-GCN and $\text{TiO}_2/\text{WS-GCN}$, inset in (e) is the pore size distributions. The fractions of WS-GCN in TiO_2 are 3 wt% for all $\text{TiO}_2/\text{WS-GCN}$ samples.

transfer of photoinduced electrons between the interfaces and to enhance photocatalytic activity.

We performed the degradation reaction of gaseous nitric oxide (NO) to evaluate the photocatalytic activity of the $\text{TiO}_2/\text{WS-GCN}$ photocatalysts. It is in stark contrast to bulk GCN that WS-GCN endowed a great enhancement of NO-degradation under simulated solar irradiation (Fig. 8a), notably in visible region, benefiting from the stronger

light-harvesting of WS-GCN with efficient enhancement of photo-induced electrons migration between WS-GCN and TiO_2 (Fig. 8b). To define incidence (λ)-dependent photodegradation activity, monochromatic lights with ascending wavelength were employed. As depicted in Fig. 8c, it maintained a high efficiency of around 60% up to 550 nm for $\text{TiO}_2/\text{WS-GCN}$ composite, and near 10% of NO degradation were still detected at 650 nm illumination. In contrast, bulk GCN just enabled a

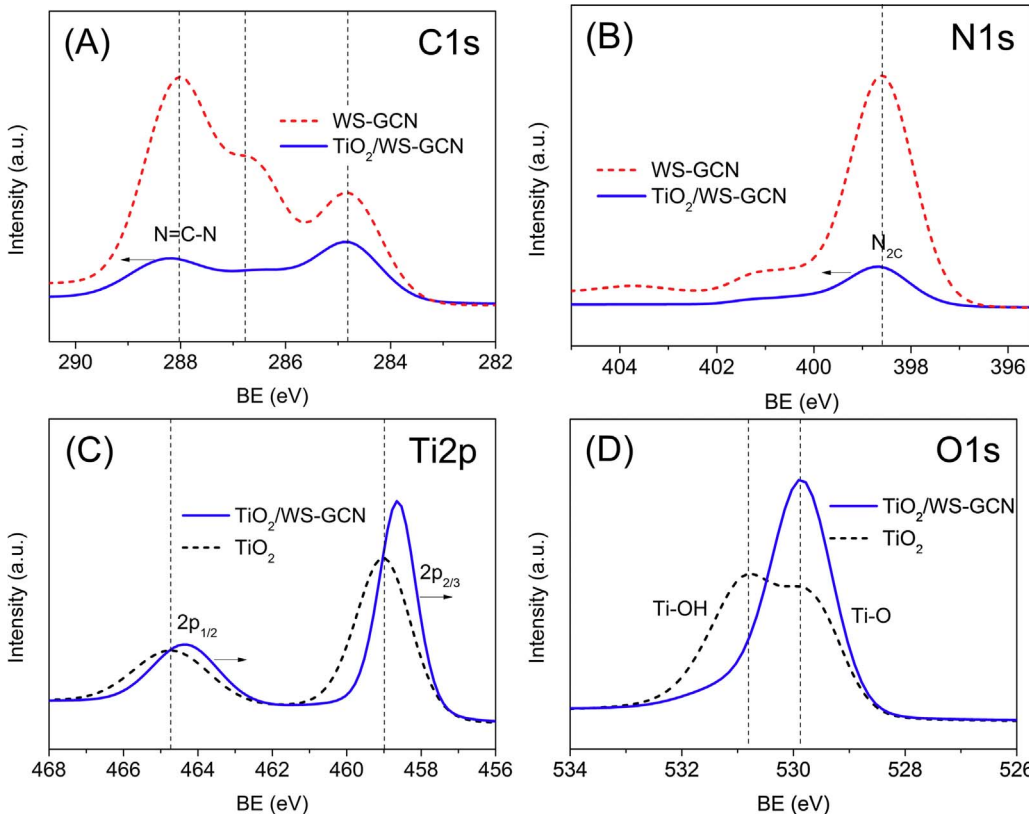


Fig. 7. (a) C 1s, (b) N 1s, (c) Ti 2p and (d) O 1s XPS spectra of $\text{TiO}_2/\text{WS-GCN}$, and the dotted lines are WS-GCN (red) and TiO_2 (black) for comparison.

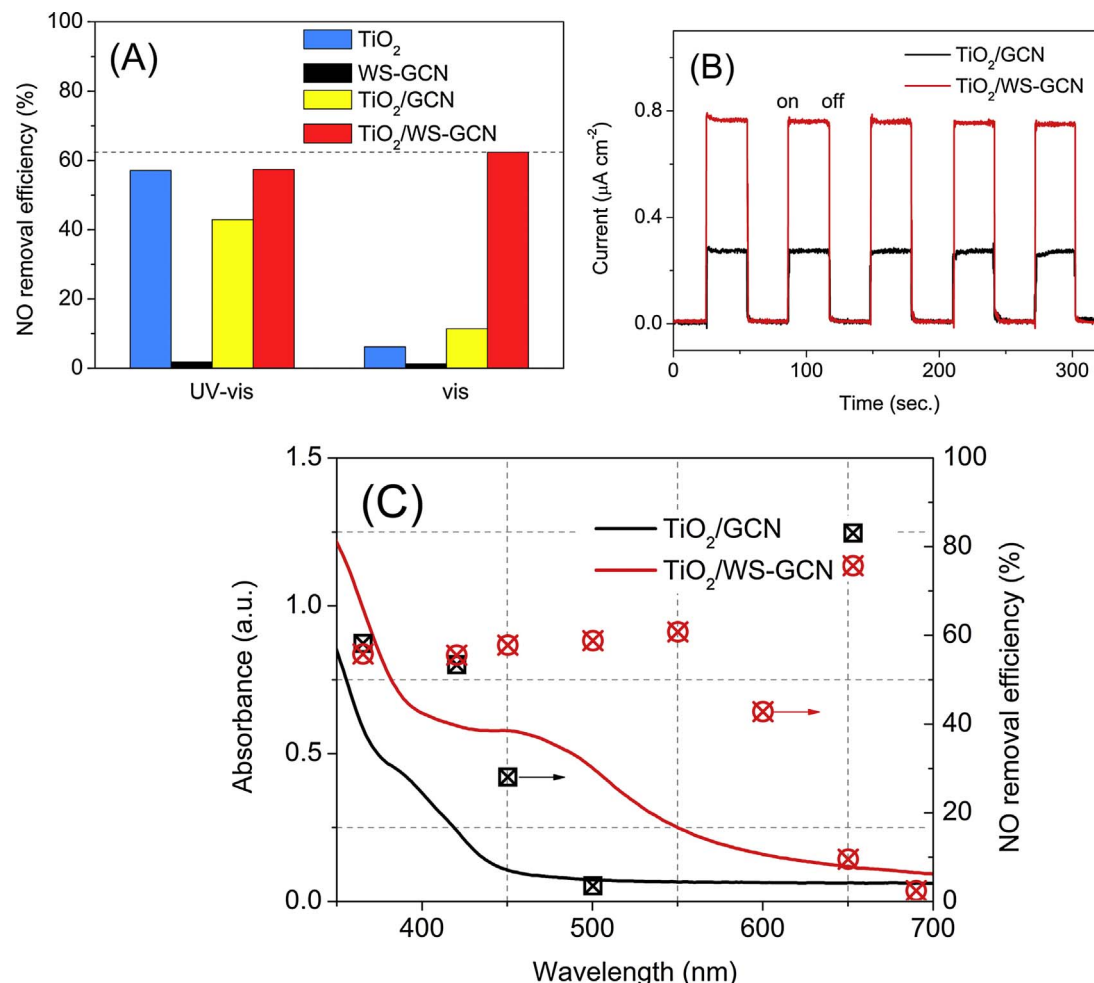


Fig. 8. Photocatalytic degradation of NO under (a) full-spectrum of a 300 W Xe lamp with AM 1.5 filter (noted as UV-vis) and visible light with both AM 1.5 and 420 cutoff filter (noted as vis), (b) contrast of transient photocurrent for TiO_2/GCN and $\text{TiO}_2/\text{WS-GCN}$ under vis-light, (c) NO removal efficiency vs irradiation wavelength using 12 W LED lamps as monochromatic light.

limited enhancement in photocatalytic efficiency over 450 nm. When exposed over 500 nm, GCN no longer contribute to photocatalytic activity. This is due to its broader intrinsic band gap than that of WS-GCN (Fig. 6f). Noting that the change of photodegradation levels for NO is closely related to the UV-vis absorbance of the photocatalyst, suggesting the photocatalysis was driven by photo-chemical energy conversion. Fig. 9a shows a single degradation curve upon $\text{TiO}_2/\text{WS-GCN}$ and the counterparts under 550 nm-irradiation. For $\text{TiO}_2/\text{WS-GCN}$, the NO concentration exhibited immediately drop from 1000 ppb after light was turned on and built a balance at about 400 ppb. At the same time, the increase of NO_2 that acts as the intermediate product during photocatalysis was very faint, indicating that the degradation reactions is fast and thoroughly. No distinct activity decay was observed after three recycling runs and a continuous 24-h test (Fig. 9b and c), indicating the material is very stable with exposed upon visible light. Interesting is, using pure WS-GCN in the same experimental conditions, or incorporation WS-GCN in SiO_2 NPs as photocatalyst, only trace amount of NO removal were detected for both of them (Fig. 8a and Fig. S10). On the other hand, when replacing anatase by brookite TiO_2 , the photocatalytic activity exhibited the similarly high level, which indicates that the excellent photocatalytic activities of $\text{TiO}_2/\text{WS-GCN}$ should be attributed to the appropriate carrier-separation as a result of strong π -d interaction and band alignment between WS-GCN and TiO_2 in present catalyst system.

3.4. Regulatory mechanisms of strong fluorescence and efficient photocatalysis

To define characterizations of semiconductor types and to determine the exact band structures, Mott-Schottky measurements were performed for WS-GCN and TiO_2 (Fig. 10a). The Mott-Schottky plots of WS-GCN and TiO_2 display a positive slope, indicating the n-type semiconductor of the both. The Mott-Schottky plots further suggest that the conduction band of WS-GCN is slightly higher than that of TiO_2 , by 0.04 V, which favors the migration of photoinduced electrons from WS-GCN to TiO_2 . The potentials vs SCE were converted to the normal hydrogen electrode (NHE) using the equation: $V_{\text{NHE}} = V_{\text{SCE}} + V_{\text{SCE}/\text{NHE}}^0$ ($V_{\text{SCE}/\text{NHE}}^0$ is 0.245 V at 25 °C). Then the conduction bands and valence band versus NHE respectively were determined by the relationship of $E_g = E_{\text{CB}} - E_{\text{VB}}$ [63], as plotted in Fig. 10b. Based on these results, we explain the photoluminescence and photocatalytic reaction process as follows (Fig. 11a). When bare WS-GCN was irradiated, the vanish of photocatalytic activity can be attributed to the result of extremely short electron life-time, 2.2 ns (Fig. 11b and Table S2), leading to the immediately returning of excited electrons to ground state toward recombination and spontaneously strong luminescent emission. For the $\text{TiO}_2/\text{WS-GCN}$ photocatalyst illuminated with visible light, the WS-GCN is excited to generate electron-hole pairs, and then photoinduced electrons migrate from the CB of WS-GCN to the CB of TiO_2 benefiting from closely attached of WS-GCN layers to the surface of TiO_2 NPs and the well matched band alignments, which allow the efficient separation of carriers and hinder recombination. The

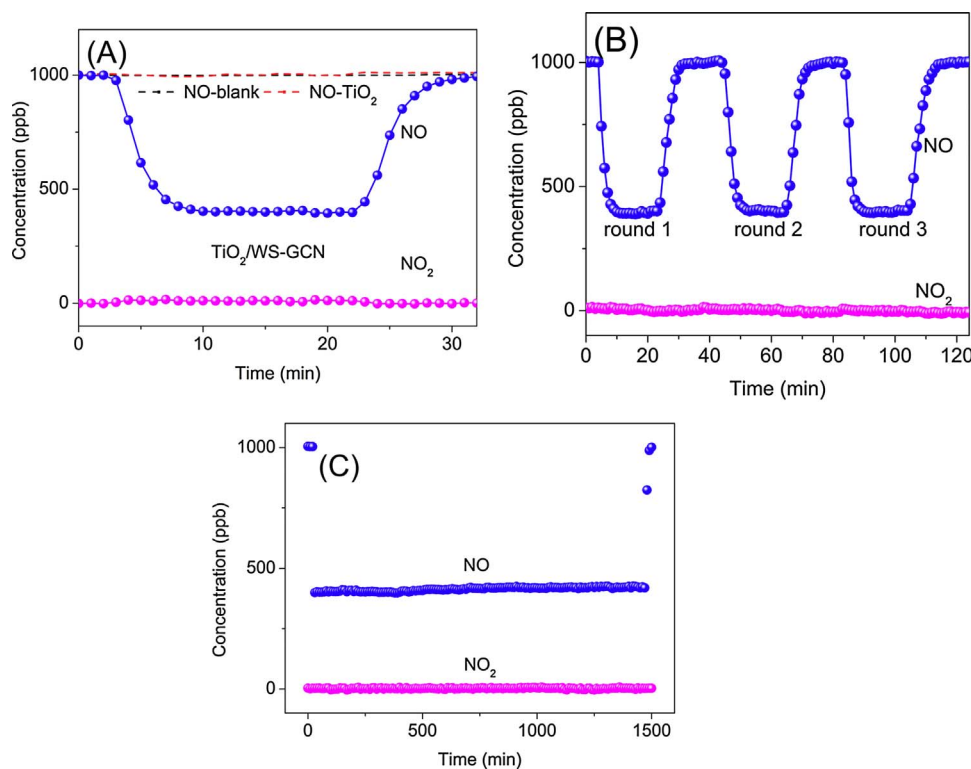


Fig. 9. NO photocatalytic degradation of the products under 550 nm monochromatic light irradiation. (a) Single process contrast, (b) 3-cycled and (c) 24 h-photocatalysis.

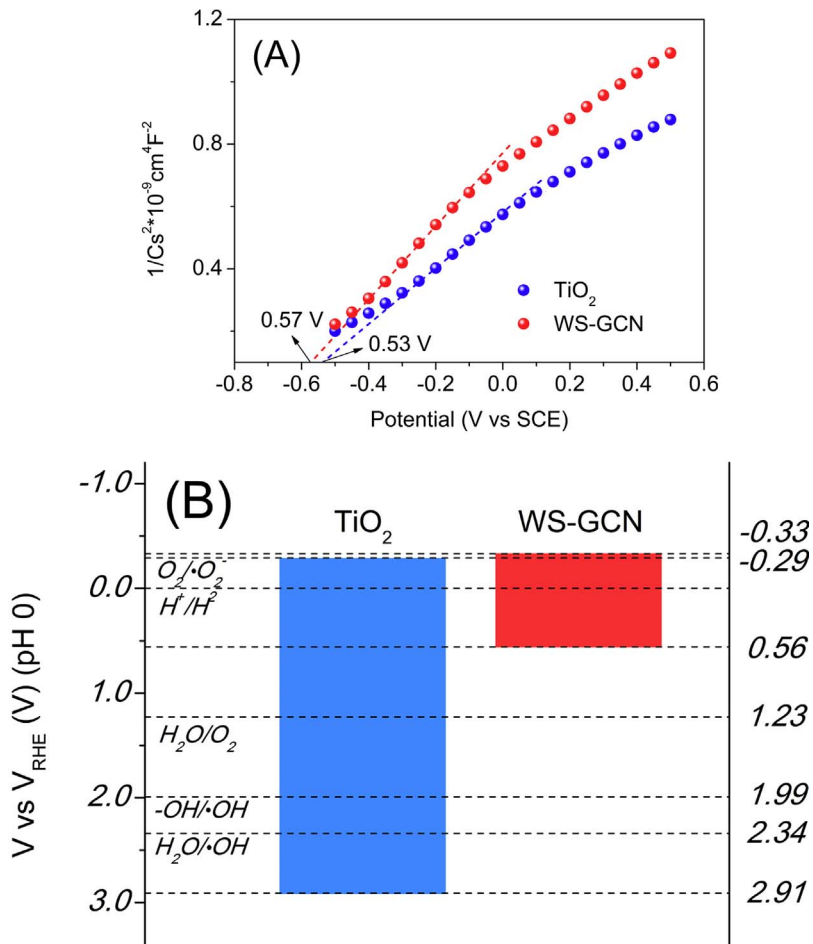


Fig. 10. (a) Mott-Schottky analysis of TiO_2 and WS-GCN showing the difference in flat band potentials and (b) the corresponding energy band diagram.

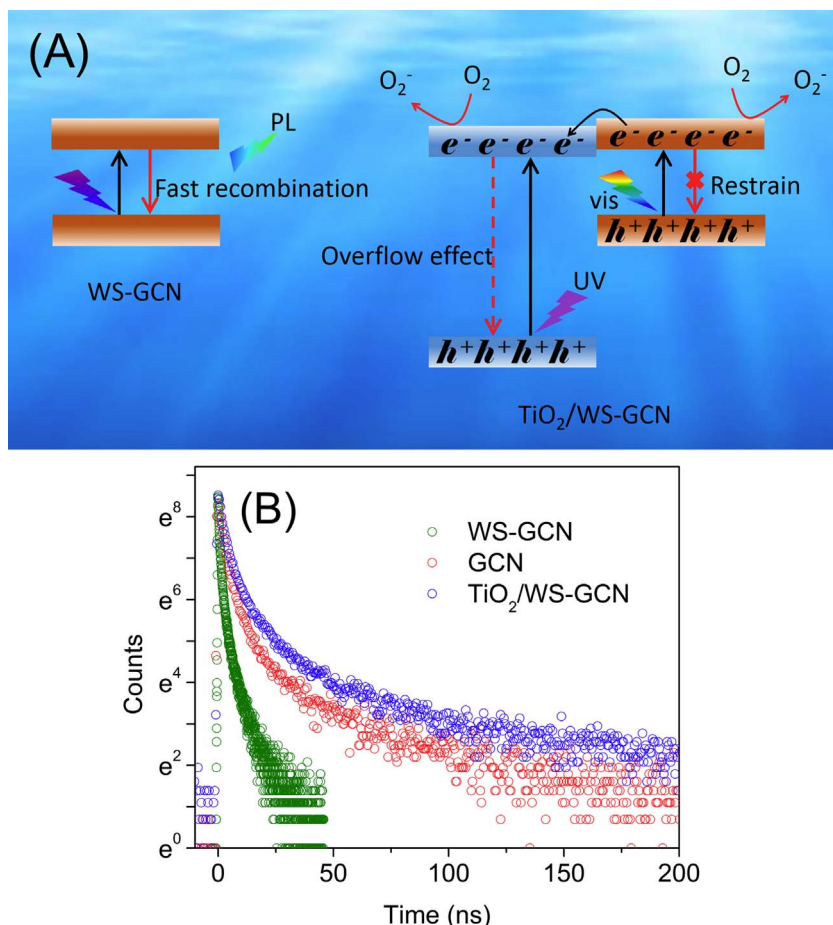


Fig. 11. (a) Possible photo-luminescence/catalysis mechanism under UV and visible light, (b) Time-resolved fluorescence spectra monitored under 375 nm laser excitation and 500 nm emission detection at room temperature for GCN, WS-GCN and $\text{TiO}_2/\text{WS-GCN}$.

longer-lived (14.8 ns) electron-hole pairs then react with the adsorbed oxidants/reducers to produce active oxygen relevant radicals (Fig. 11b), which subsequently cause degradation of the input NO gas. Significantly, the electrons might be shuttled freely along the interfaces of the nanojunction, owing to the C-rich surface of the WS-GCN in atomic-scale. In addition, no further increase of photocatalytic activity was obtained for $\text{TiO}_2/\text{WS-GCN}$ under UV light irradiation (365 nm). This could be due to simultaneous excitation of TiO_2 and WS-GCN, causing the overflow effect on CB of TiO_2 , and the electrons on the CB of TiO_2 easily recombine with the holes on the VB of TiO_2 [59].

4. Conclusion

In summary, we have demonstrated a facile one-step melt salts-assisted synthesis of high-quality water-soluble graphite carbon nitride (WS-GCN), which exhibit stable and strong photoluminescence with high absolute quantum yield (AQY) of 22%. By combining multi-superiorities of freely dispersion in water, size- and surface defect-dependent band engineering, and controllable PL properties, WS-GCN may provide a new type of fluorescent markers as well as a new approach to high-efficiency photocatalyst design for applications in bioscience, secrecy and energy-conversion technology.

Acknowledgements

This work was supported by Beijing Natural Science Foundation (2151001, 2154043), National Natural Science Foundation (51534009, 52621003, 51402008, 51225402), Scientific Research Project of Beijing Municipal Education Commission (KM201610005026), the New Century National Hundred, Thousand and Ten Thousand Talent Project, and Beijing municipal high level innovative team building program

(No. IDHT 20170502). Authors appreciate the help of Prof. Ge Chen (College of Environmental and Energy Engineering, Beijing University of Technology) on photoelectrochemical measurements.

Appendix A. Supplementary data

Supplementary data associated with this article can be found, in the online version, at <https://doi.org/10.1016/j.apcatb.2017.12.017>.

References

- [1] Y. Wang, X.C. Wang, M. Antonietti, Polymeric graphitic carbon nitride as a heterogeneous organocatalyst: from photochemistry to multipurpose catalysis to sustainable chemistry, *Angew. Chem. Int. Ed.* 51 (2012) 68–89.
- [2] J. Liu, H.Q. Wang, M. Antonietti, Graphitic carbon nitride “reloaded”: emerging applications beyond (photo)catalysis, *Chem. Soc. Rev.* 45 (2016) 2308–2326.
- [3] Y.Y. Zhang, Z.X. Zhou, Y.F. Shen, Q. Zhou, J.H. Wang, A.R. Liu, S.Q. Liu, Y.J. Zhang, Reversible assembly of graphitic carbon nitride 3D network for highly selective dyes absorption and regeneration, *ACS Nano* 10 (2016) 9036–9043.
- [4] Z.X. Zhou, J.H. Wang, J.C. Yu, Y.F. Shen, Y. Li, A.R. Liu, S.Q. Liu, Y.J. Zhang, Dissolution and liquid crystals phase of 2D polymeric carbon nitride, *J. Am. Chem. Soc.* 137 (2015) 2179–2182.
- [5] Y.J. Zhang, T. Mori, J.H. Ye, Polymeric carbon nitrides: semiconducting properties and emerging applications in photocatalysis and photoelectrochemical energy conversion, *Sci. Adv. Mater.* 4 (2012) 282–291.
- [6] G.G. Liu, T. Wang, H.B. Zhang, X.G. Meng, D. Hao, K. Chang, P. Li, T. Kako, J.H. Ye, Nature-Inspired environmental phosphorylation boosts photocatalytic H_2 production over carbon nitride nanosheets under visible-light irradiation, *Angew. Chem.* 127 (2015) 1–6.
- [7] X.J. Bai, L. Wang, R.L. Zong, Y.F. Zhu, Photocatalytic activity enhanced via g-C₃N₄ nanoplates to nanorods, *J. Phys. Chem. C* 117 (2013) 9952–9961.
- [8] F.Z. Su, S.C. Mathew, G. Lipner, X.Z. Fu, M. Antonietti, S. Blechert, X.C. Wang, MpG-C₃N₄-catalyzed selective oxidation of alcohols using O_2 and visible light, *J. Am. Chem. Soc.* 132 (2010) 16299–16301.
- [9] D. Yue, X. Qian, Y. Zhao, Photocatalytic remediation of ionic pollutant, *Sci. Bull.* 60 (2015) 1791–1806.
- [10] Y.W. Yuan, L.L. Zhang, J. Xing, M.I.B. Utama, X. Lu, K. Du, Y.M. Li, X. Hu,

- S.J. Wang, A.G.R. Dunin-Borkowski, J. Arbiold, Q.H. Xiong, High-yield synthesis and optical properties of g-C₃N₄, *Nanoscale* 7 (2015) 12343–12350.
- [11] Y.F. Zhao, R.Y. Wei, X. Feng, L.N. Sun, P.P. Liu, Y.X. Su, L.Y. Shi, Dual-mode luminescent nanopaper based on ultrathin g-C₃N₄ nanosheets grafted with rare-earth upconversion nanoparticles, *ACS Appl. Mater. Inter.* 8 (2016) 21555–21562.
- [12] H. Li, M.M. Yang, J. Liu, Y.L. Zhang, Y.M. Yang, H. Huang, Y. Liu, Z.H. Kang, A practical and highly sensitive C₃N₄-TYR fluorescent probe for convenient detection of dopamine, *Nanoscale* 7 (2015) 12068–12075.
- [13] Y.P. Wang, Y.K. Li, W. Ju, J.C. Wang, H.C. Yao, L. Zhang, J.S. Wang, Z.J. Li, Molten salt synthesis of water-dispersible polymeric carbon nitride nanoseaweeds and their application as luminescent probes, *Carbon* 102 (2016) 477–486.
- [14] H.Y. Chen, L.W. Ruan, X. Jiang, L.G. Qiu, Trace detection of nitro aromatic explosives by highly fluorescent g-C₃N₄ nanosheets, *Analyst* 140 (2015) 637–643.
- [15] X.D. Zhang, X. Xie, H. Wang, J.J. Zhang, B.C. Pan, Y. Xie, Enhanced photoresponsive ultrathin graphitic-phase C₃N₄ nanosheets for bioimaging, *J. Am. Chem. Soc.* 135 (2013) 18–21.
- [16] X.D. Zhang, H.X. Wang, H. Wang, Q. Zhang, J.F. Xie, Y.P. Tian, J. Wang, Y. Xie, Single-layered graphitic-C₃N₄ quantum dots for two-photon fluorescence imaging of cellular nucleus, *Adv. Mater.* 26 (2014) 4438–4443.
- [17] A.J. Wang, H. Li, H. Huang, Z.S. Qian, J.J. Feng, Fluorescent graphene-like carbon nitrides: synthesis, properties and applications, *J. Mater. Chem. C* 4 (2016) 8146–8160.
- [18] C. Zhou, Y.M. Chen, P.X. Shang, Y.W. Chi, Strong electrochemiluminescent interactions between carbon nitride nanosheet-reduced graphene oxide nanohybrids and folic acid, and ultrasensitive sensing for folic acid, *Analyst* 141 (2016) 3379–3388.
- [19] L.L. Feng, F. He, B. Liu, G.X. Yang, S.L. Gai, P.P. Yang, C.X. Li, Y.L. Dai, R.C. Lv, J. Lin, G-C₃N₄ coated upconversion nanoparticles for 808 nm near-Infrared light triggered phototherapy and multiple imaging, *Chem. Mater.* 28 (2016) 7935–7946.
- [20] M. Chan, C.W. Chen, I. Lee, Y.C. Chan, D.T. Tu, M. Hsiao, C.H. Chen, X.Y. Chen, R.S. Liu, Near-infrared light-mediated photodynamic therapy nanoplatform by the electrostatic assembly of upconversion nanoparticles with graphitic carbon nitride quantum dots, *Inorg. Chem.* 55 (2016) 10267–10277.
- [21] G.H. Dong, L.Z. Zhang, Synthesis and enhanced Cr(VI) photoreduction property of formate anion containing graphitic carbon nitride, *J. Phys. Chem. C* 117 (2013) 4062–4068.
- [22] Y.J. Zhang, A. Thomas, M. Antonietti, X.C. Wang, Activation of carbon nitride solids by protonation: morphology changes, enhanced ionic conductivity, and photoconduction experiments, *J. Am. Chem. Soc.* 131 (2009) 50–51.
- [23] X.C. Wang, K. Maeda, X.F. Chen, K. Takanabe, K. Domen, Y.D. Hou, X.Z. Fu, M. Antonietti, Polymer semiconductors for artificial photosynthesis: hydrogen evolution by mesoporous graphitic carbon nitride with visible light, *J. Am. Chem. Soc.* 131 (2009) 1680–1681.
- [24] S.X. Min, G.X. Lu, Enhanced electron transfer from the excited eosin Y to mpg-C₃N₄ for highly efficient hydrogen evolution under 550 nm irradiation, *J. Phys. Chem. C* 116 (2012) 19644–19652.
- [25] Y.H. Zhang, Q.W. Pan, G.Q. Chai, M. Liang, G.P. Dong, Q.Y. Zhang, J.R. Qiu, Synthesis and luminescence mechanism of multicolor-emitting g-C₃N₄ nanopowders by low temperature thermal condensation of melamine, *Sci. Rep.* 3 (2013) 1943–1940.
- [26] A.B. Jorge, D.J. Martin, M.T.S. Dhanoa, A.S. Rahman, N. Makwana, J. Tang, A. Sella, F. Corà, S. Firth, J.A. Darr, P.F. McMillan, H₂ and O₂ evolution from water half-splitting reactions by graphitic carbon nitride materials, *J. Phys. Chem. C* 117 (2013) 7178–7185.
- [27] J. Chen, D. Zhao, Z. Diao, M. Wang, S. Shen, Ferrites boosting photocatalytic hydrogen evolution over graphitic carbon nitride: a case study of (Co Ni)Fe₂O₄ modification, *Sci. Bull.* 61 (2016) 292–301.
- [28] Q. Hao, X.X. Niu, C.S. Nie, S.M. Hao, W. Zou, J.M. Ge, D.M. Chen, W.Q. Yao, A highly efficient g-C₃N₄/SiO₂ heterojunction: the role of SiO₂ in the enhancement of visible light photocatalytic activity, *Phys. Chem. Chem. Phys.* 18 (2016) 31410–31418.
- [29] Q. Hao, S.M. Hao, X.X. Niu, X. Li, D.M. Chen, H. Ding, Enhanced photochemical oxidation ability of carbon nitride by π-π stacking interactions with graphene, *Chin. J. Catal.* 38 (2017) 278–286.
- [30] Q. Hao, R.T. Wang, H.J. Lu, C.A. Xie, Y.F. Zhu, One-pot synthesis of C/Bi/Bi₂O₃ composite with enhanced photocatalytic activity, *Appl. Catal. B: Environ.* 219 (2017) 63–72.
- [31] S.B. Yang, Y.J. Gong, J.H. Zhang, L. Zhan, L.L. Ma, Z.Y. Fang, R. Vajtai, X.C. Wang, P.M. Ajayan, Exfoliated graphitic carbon nitride nanosheets as efficient catalysts for hydrogen evolution under visible light, *Adv. Mater.* 25 (2013) 2452–2456.
- [32] J. Xu, L.W. Zhang, R. Shi, Y.F. Zhu, Chemical exfoliation of graphitic carbon nitride for efficient heterogeneous photocatalysis, *J. Mater. Chem. A* 1 (2013) 14766–14772.
- [33] P. Niu, L.L. Zhang, G. Liu, H.M. Cheng, Graphene-like carbon nitride nanosheets for improved photocatalytic activities, *Adv. Funct. Mater.* 22 (2012) 4763–4770.
- [34] X.J. Bai, C.P. Sun, S.L. Wu, Y.F. Zhu, Enhancement of photocatalytic performance via a P3HT-g-C₃N₄ heterojunction, *J. Mater. Chem. A* 3 (2015) 2741–2747.
- [35] J.S. Zhang, M.W. Zhang, S. Lin, X.Z. Fu, X.C. Wang, Molecular doping of carbon nitride photocatalysts with tunable bandgap and enhanced activity, *J. Catal.* 310 (2014) 24–30.
- [36] X.C. Wang, X.F. Chen, A. Thomas, X.Z. Fu, M. Antonietti, Metal-containing carbon nitride compounds: a new functional organic-metal hybrid material, *Adv. Mater.* 21 (2009) 1609–1612.
- [37] B. Kurpil, A. Savateev, V. Papaefthimiou, S. Zafeiratos, T. Heil, S. Özenler, D. Dontsova, M. Antonietti, Hexaazatriphenylene doped carbon nitrides—Biomimetic photocatalyst with superior oxidation power, *Appl. Catal. B: Environ.* 217 (2017) 622–628.
- [38] P. Niu, L.C. Yin, Y.Q. Yang, G. Liu, H.M. Cheng, Increasing the visible light absorption of graphitic carbon nitride (Melon) photocatalysts by homogeneous self-modification with nitrogen vacancies, *Adv. Mater.* 26 (2014) 8046–8052.
- [39] Z.Z. Lin, X.C. Wang, Nanostructure engineering and doping of conjugated carbon nitride semiconductors for hydrogen photosynthesis, *Angew. Chem. Int. Ed.* 52 (2013) 1735–1738.
- [40] Z.X. Pei, J.X. Gu, Y.K. Wang, Z.J. Tang, Z.X. Liu, Y. Huang, Y. Huang, J.X. Zhao, Z.F. Chen, C.Y. Zhi, Component matters paving the roadmap toward enhanced electrocatalytic performance of graphitic C₃N₄-based catalysts via atomic tuning, *ACS Nano* 11 (2017) 6004–6014.
- [41] J.S. Zhang, M.W. Zhang, R.Q. Sun, X.C. Wang, A facile band alignment of polymeric carbon nitride semiconductors to construct isotype heterojunctions, *Angew. Chem. Int. Ed.* 124 (2012) 10292–10296.
- [42] J.S. Zhang, M.W. Zhang, G.G. Zhang, X.C. Wang, Synthesis of carbon nitride semiconductors in sulfur flux for water photoredox catalysis, *ACS Catal.* 2 (2012) 940–948.
- [43] G. Liu, P. Niu, C.H. Sun, S.C. Smith, Z.G. Chen, G.Q. Lu, H.M. Cheng, Unique electronic structure induced high photoreactivity of sulfur-doped graphitic C₃N₄, *J. Am. Chem. Soc.* 132 (2010) 11642–11648.
- [44] Y.J. Zhang, T. Mori, J.H. Ye, M. Antonietti, Phosphorus-doped carbon nitride solid: enhanced electrical conductivity and photocurrent generation, *J. Am. Chem. Soc.* 132 (2010) 6294–6295.
- [45] X.G. Ma, Y.H. Lv, J. Xu, Y.F. Liu, R.Q. Zhang, Y.F. Zhu, A strategy of enhancing the photoactivity of g-C₃N₄ via doping of nonmetal elements: a first-principles study, *J. Phys. Chem. C* 116 (2012) 23485–23493.
- [46] T. Xiong, W.L. Cen, Y.X. Zhang, F. Dong, Bridging the g-C₃N₄ interlayers for enhanced photocatalysis, *ACS Catal.* 6 (2016) 2462–2472.
- [47] Y.X. Li, H. Xu, S.X. Ouyang, D. Lu, X. Wang, D.F. Wang, J.H. Ye, In situ surface alkalinized g-C₃N₄ toward enhancement of photocatalytic H₂ evolution under visible-light irradiation, *J. Mater. Chem. A* 4 (2016) 2943–2950.
- [48] M. Wu, J.M. Yan, X.N. Tang, M. Zhao, Q. Jiang, Synthesis of potassium-modified graphitic carbon nitride with high photocatalytic activity for hydrogen evolution, *ChemSusChem* 7 (2014) 2654–2658.
- [49] J.M. Luo, G.H. Dong, Y.Q. Zhu, Z. Yang, C.Y. Wang, Switching of semiconducting behavior from n-type to p-type induced high photocatalytic NO removal activity in g-C₃N₄, *Appl. Catal. B: Environ.* 214 (2017) 46–56.
- [50] Y. Wang, Y. Di, M. Antonietti, H.R. Li, X.F. Chen, X.C. Wang, Excellent visible-light photocatalysis of fluorinated polymeric carbon nitride solids, *Chem. Mater.* 22 (2010) 5119–5121.
- [51] J.W. Fang, H.Q. Fan, M.M. Li, C.B. Long, Nitrogen self-doped graphitic carbon nitride as efficient visible light photocatalyst for hydrogen evolution, *J. Mater. Chem. A* 3 (2015) 13819–13826.
- [52] G.P. Mane, S.N. Talapaneni, K.S. Lakhi, H. Ilbeygi, U. Ravon, K. AlBahily, T. Mori, D. Park, A. Vinu, Highly ordered nitrogen-rich mesoporous carbon nitrides and their superior performance for sensing and photocatalytic hydrogen generation, *Angew. Chem. Int. Ed.* 56 (2017) 1–6.
- [53] L.B. Jiang, X.Z. Yuana, Y. Pan, J. Liang, G.M. Zeng, Z.B. Wu, H. Wang, Doping of graphitic carbon nitride for photocatalysis: a review, *Appl. Catal. B: Environ.* 217 (2017) 388–406.
- [54] P. Niu, G. Liu, H.M. Cheng, Nitrogen vacancy-promoted photocatalytic activity of graphitic carbon nitride, *J. Phys. Chem. C* 116 (2012) 11013–11018.
- [55] H.J. Yu, R. Shi, Y.X. Zhao, T. Bian, Y.F. Zhao, C. Zhou, G.I.N. Waterhouse, L.Z. Wu, C.H. Tung, T.R. Zhang, Alkali-assisted synthesis of nitrogen deficient graphitic carbon nitride with tunable band structures for efficient visible-light-driven hydrogen evolution, *Adv. Mater.* 29 (2017) 1605148.
- [56] Y.Y. Kang, Y.Q. Yang, L.C. Yin, X.D. Kang, G. Liu, H.M. Cheng, An amorphous carbon nitride photocatalyst with greatly extended visible-light-responsive range for photocatalytic hydrogen generation, *Adv. Mater.* 27 (2015) 4572–4577.
- [57] J.J. Li, Y.M. Zhang, X.H. Zhang, J.C. Han, Y. Wang, L. Gu, Z.H. Zhang, X.J. Wang, J.K. Jian, P. Xu, B. Song, Direct transformation from graphitic C₃N₄ to nitrogen-doped graphene: an efficient metal-free electrocatalyst for oxygen reduction reaction, *ACS Appl. Mater. Inter.* 7 (2015) 19626–19634.
- [58] H.F. Lin, L.P. Li, M.L. Zhao, X.S. Huang, X.M. Chen, G.S. Li, R.C. Yu, Synthesis of high-quality brookite TiO₂ single-crystalline nanosheets with specific facets exposed: tuning catalysts from inert to highly reactive, *J. Am. Chem. Soc.* 134 (2012) 8328–8331.
- [59] J.G. Yu, J.X. Low, W. Xiao, P. Zhou, M. Jaroniec, Enhanced photocatalytic CO₂-reduction activity of anatase TiO₂ by coexposed {001} and {101} facets, *J. Am. Chem. Soc.* 136 (2014) 8839–8842.
- [60] Y.L. Li, J.S. Wang, Y.L. Yang, Y. Zhang, D. He, Q. An, G.Z. Cao, Seed-induced growing various TiO₂ nanostructures on g-C₃N₄ nanosheets with much enhanced photocatalytic activity under visible light, *J. Hazard. Mater.* 292 (2015) 79–89.
- [61] J.S. Zhang, M.W. Zhang, L.H. Lin, X.C. Wang, Sol processing of conjugated carbon nitride powders for thin-film fabrication, *Angew. Chem. Int. Ed.* 54 (2015) 1–6.
- [62] L.W. Zhang, H.B. Fu, Y.F. Zhu, Efficient TiO₂ photocatalysts from surface hybridization of TiO₂ particles with graphite-like carbon, *Adv. Funct. Mater.* 18 (2008) 2180–2189.
- [63] C.C. Dong, Z.Y. Ma, R.T. Qie, X.H. Guo, C.H. Li, R.J. Wang, Y.L. Shi, B. Dai, X. Jia, Morphology and defects regulation of carbon nitride by hydrochloric acid to boost visible light absorption and photocatalytic activity, *Appl. Catal. B: Environ.* 217 (2017) 629–636.